The corrosion resistance of dental Ti6Al4V with differing microstructures in oral environments

Mirjam Bajt Leban [a,*], *Tadeja Kosec* [a], *Matjaž Finšgar* [b]

[a] Slovenian National Building and Civil Engineering Institute, Dimičeva 12, 1000 Ljubljana, Slovenia
[b] University of Maribor, Faculty of Chemistry and Chemical Engineering, 2000 Maribor, Slovenia

ARTICLE INFO

ABSTRACT

The impact of the microstructural properties of a Ti6Al4V alloy on its electrochemical properties, as well as the effect of the α- and β-phases present within it, is still unclear. With the introduction of new, emerging technologies, such as selective laser melting and post heat treatments, the effect of the microstructure on an alloy's corrosion properties has become increasingly interesting from a scientific perspective. When these alloys are produced through different methods, despite an identical chemical composition they have diverse microstructures, and consequently display varying resistance to corrosion. In the present research study, Ti−6Al−4V alloy specimens produced by three different processes, leading to the formation of three different microstructures were investigated: heat treated specimen fabricated by selective laser melting, wrought and cast specimens. The impact of the microstructure of these alloys when immersed in artificial saliva was studied through the use of various electrochemical techniques, by microscopical examinations, and time-of-flight secondary ion mass spectrometry. Corrosion properties were investigated by the measurement of open circuit potential, linear polarization, and potentiodynamic curve measurements followed by microscopical examinations, and time-of-flight secondary ion mass spectrometry examination was conducted to reveal spatial distribution of alloying species on oxide film. It was found that the difference between specimens containing an α+β microstructure was small and not dependent on the aspect ratio of the β-phase, alloy grain size, and vanadium partitioning coefficient, but rather on the size, shape, and content of this phase.

1. Introduction

Ti6Al4V alloys possess high specific strength and corrosion resistance, classifying them as suitable for use in the aerospace, automotive, and chemical industries, as well as in medicine [1−4]. Ti6Al4V alloys are widely used in medicine, mainly due to their excellent mechanical and corrosion properties as well as their biocompatibility. For this reason, these alloys are also used for dental implants, posts, and cores, where the constantly changing and demanding environment within the oral cavity presents a major challenge [5−8].

For decades, wrought and cast products made from Ti6Al4V alloy have been the primary material used in dental technology. Wrought discs and rods are machined into the

---

desired shape by milling, while cast products are manufactured in laboratories by investment casting in waxes, usually under vacuum [9]. The evolution of digital technology and the development of computer aided design/manufacturing (CAD/CAM) in the 1960's set a milestone for automated manufacturing processes [10], enabling the production of 3D objects by metal powder-based additive manufacturing (AM), in addition to the previously-used manufacturing processes involving casting or milling and turning from larger prefabricated blocks [10—12]. AM is a process whereby components are built directly, by slicing a solid model into multiple layers; the product is then built layer by layer, using a laser or electron beam in a computer-controlled printing machine to melt the powder [13].

The use of varying manufacturing paths in the production of Ti6Al4V alloys, which can differ in terms of the temperature and cooling rate used and the simultaneous presence of mechanical loads, impacts the mechanical and microstructural properties of the end products. Ti6Al4V alloy is one of the so-called $\alpha+\beta$ alloys, where the α-phase is stabilized by Al and the β-phase by V. The thermomechanical history of this alloy, however, influences the formation of its final microstructure. It defines the type, size and morphology of the phases present [14]. The microstructure of a Ti6Al4V alloy fabricated by selective laser melting (SLM), one of the AM powder bed processes, primarily contains martensitic α' (hcp), due to the very high cooling rates (over 410 °C/s) that occur during solidification [15]. The ductility of this type of alloy is not sufficient for many applications. For this reason, these alloys are usually heat-treated in order to improve their mechanical properties. Heat treating an α' martensitic alloy to temperatures above β-transus, followed by slow cooling and/or additional ageing, leads to decomposition of α' (hcp), to α (hcp) and β (bcc) phases [16]. α- and β-phases are also the main phases of wrought and cast alloys, but the morphology of these two phases differs significantly. Wrought alloy has a homogeneous microstructure, containing equiaxed α-phase with β-phase on the grain boundaries [17]. Cast alloy, on the other hand, consists of a Widmanstätten $\alpha+\beta$ microstructure [18].

The excellent corrosion resistance of a Ti6Al4V alloy is enabled by the instantaneous formation of a protective oxide layer in the presence of an oxidative atmosphere. This protective layer is a few nanometers thick and mainly composed of TiO_2, with a minority of other suboxides. Oral environments, saliva [19], however, contain a complex mixture of aggressive ions that can cause corrosion. Under certain circumstances, for example, inflammatory processes of the tissue, even acidic, can be very corrosive and could cause the mechanical failure of a metallic material, and also the unwanted migration of toxic or allergen species into the human body [20—24]. It has been shown that the differences in corrosion resistance that exist between various Ti6Al4V alloys are primarily dependent on their microstructure. Qin et al. [25] thus concluded that the corrosion resistance of Ti6Al4V in a NaCl aqueous solution depends on the homogeneity of the elemental composition along the surface, which, in turn, is strongly dependent on the type and distribution of the α- and β-phases. Similar conclusions have been reported for the same alloy in a different microstructural condition in the same environment [17,26]. Chen et al. [5] found that β-phase

resists corrosion better than α-phase when immersed in a corrosive solution. Other studies [26,27], however, have reported the opposite — namely, the detrimental corrosion behavior of a Ti6Al4V alloy containing β-phase.

Based on the above, it is impossible to unequivocally conclude the influence of an individual phase on the corrosion behavior of a Ti–6Al–4V alloy in artificial saliva (AS) or a physiological solution. Moreover, no exact differences in the passive layer above the individual phases (α or β) in a $\alpha+\beta$ Ti alloy have been reported. The aim of this study was therefore to investigate the impact of α- and β-phases on the corrosion behavior of Ti6Al4V alloys manufactured by different processes when immersed in various artificial oral environments, through the implementation of electrochemical tests and surface characterization techniques. Time-of-flight secondary ion mass spectrometry (ToF-SIMS) was found to be an appropriate technique to determine the spatial distribution of constituents in the oxide layer over dual-phase Ti alloys within the microstructure.

2. Materials and methods

This study investigated Ti6Al4V alloys with three different microstructures, namely: i) selective laser melted (SLM) specimens additionally heat-treated above β-transus at 1050 °C (designated as SLM-HT), ii) wrought and iii) cast samples. Gas atomized powder for the SLM specimens was provided by S&S Scheftner GmbH. It's chemical composition was 6 % Al, 4 % V, and less than 1 % total concentration of Fe, Si, and C, with the rest being Ti (all data for chemical compositions from hereon in are reported in wt%). SLM specimens were produced using the following parameters: laser power of 60 W, laser travel velocity of 805 mm/s, and a hatch distance and layer thickness both of 25 μm. The laser energy density was calculated to be 119.3 J/mm³. Wrought specimens were made from a sheet, provided by Goodfellow (Product code Ti01-FL-000350), with a nominal chemical composition of 6 % Al, 4 % V, and the rest Ti. No data was available for Fe or any other elements. Based on the optical emission spectroscopy cast analysis, the cast specimen contained 6.20 % Al, 4.20 % V, 0.16 % Fe, and the rest Ti.

Metallographic examinations of specimens etched with Kroll (3 mL 40 % HF and 5 mL 30 % HNO_3 in 92 mL of H_2O) were performed to reveal the microstructures. The surfaces of the specimens were investigated using a metallographic-confocal microscope (Axio Imager Z2, Carl Zeiss) with Ten software. The amount of β-phase was determined from the microstructure using ImageJ software. XRD analysis was conducted using a Malvern Panalytical Empyrean diffractometer in order to quantitatively determine the microstructure. The data was analyzed using HighScore Plus database software. The spectra were measured between 2θ of 4° and 100° using a step size of 0.0065° and time per step of 61.2 ms. SEM/EDX analysis was carried out using a JEOL IT500 scanning electron microscope, an AZTEC ADV XMAX 65 EDX detector, and AZtec 4.3 software.

The electrochemical tests consisted of open circuit potential (E_{oc}) measurements over a period of 6800 s, linear polarization (LP) and potentiodynamic curve (PD) measurements. Electrochemical tests were performed using a Gamry 600+
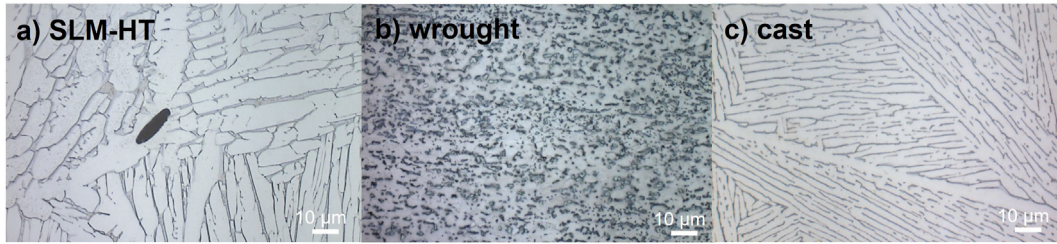
Fig. 1 – Optical micrographs of the Ti6Al4V alloys investigated: a) SLM-HT, b) wrought, and c) cast specimens.

potentiostat/galvanostat in a three electrode cell. Three different types of AS were used as the electrolytes in this study. The AS consisted of 0.6 g/L NaCl, 0.72 g/L KCl, 0.22 g/L $CaCl_2 \cdot 2H_2O$, 0.68 g/L KH_2PO_4, 0.856 g/L $Na_2HPO_4 \cdot 12H_2O$, 0.060 g/L KSCN, 1.5 g/L $KHCO_3$, and 0.03 g/L citric acid [19]. The second solution was AS 0,076 M NaF(represents the typical F^- concentration in mouthwash) [19,28]. The third solution was AS acidified with 0.1 M lactic acid. The pH values of the AS and AS with NaF were 6.9 ± 0.1, while the pH of the AS with lactic acid was 2.3 ± 0.1. Prior to each test, the surfaces of TiAlV samples were polished to a surface finish using P1200 SiC paper, which was then rinsed with distilled water and ethanol and dried in hot air.

After 2 h immersion, LP was measured in the potential range ± 10 mV/s vs E_{oc}, using a scan rate of 0.1 mV/s. Polarisation resistance (R_p) was determined from the LP measurements based on the slopes of the curves measured. PD measurements started at 0.25 V more negative than corrosion potential (E_{corr}), and progressed in the anodic direction up to 3.30 V or until the current density equalled 1 mA/cm^2 (whichever condition was reached first), using a scan rate of 1 mV/s. All tests were conducted at 37 °C.

An M6 instrument (IONTOF, Münster, Germany) was employed and controlled by SurfaceLab 7.3 software to perform ToF-SIMS imaging on spontaneously formed oxide layer on polished surfaces (0.05 μm colloidal silica) of Ti6Al4V alloys. ToF-SIMS spectra were calibrated with known peaks at certain mass-to-charge ratio (*m/z*). ToF-SIMS imaging was performed with a 30 keV Bi$^+$ as the primary beam and a target current of 1.2 pA.

3. Results

3.1. Microstructure and phase composition

Fig. 1 shows the microstructures of the Ti6Al4V alloys produced in different ways. The microstructure of the SLM-HT specimen is a mixture of coarse α + β lamellas, without prior β-grain boundaries, which were completely transformed during exposure to temperatures higher than β-transus [29]. The wrought specimen mainly consists of fine, equally-distributed equiaxed α-phase (white), with β-phase (dark) present at the boundaries [17]. The specimen produced by investment casting contains a Widmanstätten structure, consisting of alternate α-plates and β-phase in the coarse, former β-grains. Plate-shaped α-phase grain boundaries were formed when the former β-grains were slowly cooled from temperatures over β-transus to room temperature [18].

The aspect ratio of the β-phase (i.e. the ratio between the width and height of the β-phase) of the specimens investigated was calculated as the average of 20 representative phases taken from metallographic images at 1000-times magnification. The highest ratio, ~100 ± 25, was observed in
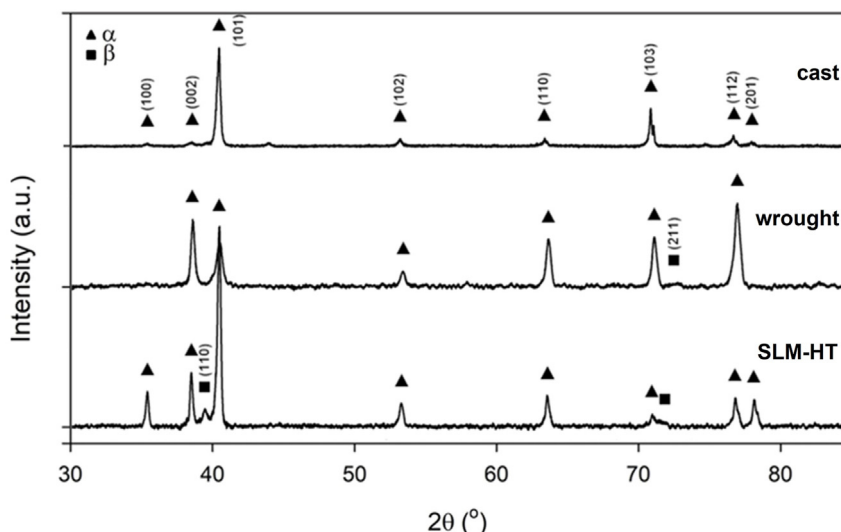
Fig. 2 – XRD diffractograms of the Ti6Al4V alloys tested.
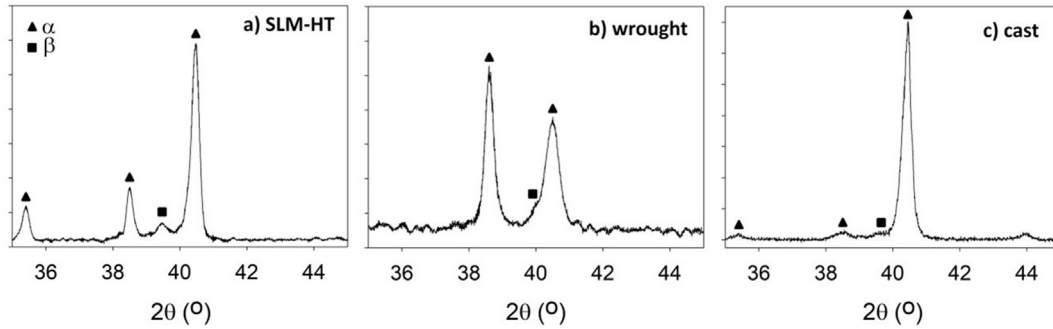
Fig. 3 – Zoomed-in XRD patterns in a 2θ range between 35° and 45°.

the cast specimen, followed by ~20 ± 10 for the SLM-HT specimen, and ~2.0 ± 0.5 for the wrought specimen.

The amount of β-phase in the SLM-HT, wrought, and cast specimens, as determined from the microstructural images, was 30.6 %, 16.4 %, and 21.3 %, respectively.

Fig. 2 shows XRD diffractograms for the Ti6Al4V alloys investigated. The SLM-HT specimen, produced by SLM with additional heat treatment at 1050 °C, contains peaks representing different crystallographic orientations of α-phase and a β-phase $(110)_\beta$ peak with a body-centred cubic structure. The XRD diffractograms in Fig. 3 show that the β peak is present in the SLM-HT specimen as well as in the wrought and cast specimens. The highest intensity was measured in the $(002)_\alpha$ and $(112)_\alpha$ peaks in the case of the wrought specimen, and in the $(101)_\alpha$ peak in the cast specimen. In the diffraction patterns of the wrought and cast specimens, the β-phase $(110)_\beta$ peak does not appear as a freestanding peak, but rather as part of the $(101)_\alpha$ peak. Of the peaks that indicate β-phase, only the $(110)_\beta$ peak is present in the XRD diffractograms for the SLM-HT and cast specimens. The other β-phase peak, $(211)_\beta$, was only detected in the wrought specimen. The β-phase content, deduced from the ratio between the sum of the areas under all the peaks, obtained by numerical integration of the difractograms [30,31], divided by the β-phase peaks, increases in the following order: cast < wrought < SLM-HT.

The chemical composition of the alloying elements Al and V in the α- and β-phases of the specimens investigated are presented in Table 1. The compositions vary due to differences in the diffusion conditions during cooling [32]. Differences in chemical composition can be indicated by the so-called elemental partitioning parameter (k_i) [33], calculated as the ratio between the composition of an alloying element (i = Al or V) in the β- ($X_{i\beta}$) and α- ($X_{i\alpha}$) phases. This parameter is presented for each of the alloys in Table 1, with the exception

of the SLM specimen, where no β-phase was present. Parameter k_i is defined as follows:

$$k_i = X_{i\beta}/X_{i\alpha} \qquad (1)$$

The composition of Al, which is an α-stabilizing element, is higher in the α-phase, but lower in the β-phase (being also lower than the Al concentration in the nominal alloy composition). The opposite was observed for V, which is a β-stabilizing element. This indicates the diffusion of Al (in the α-phase) and V (in the β-phase) during their formation and depends on the available time and temperature during solidification [32]. The solubility of V in the α-phase, however, is limited, whereas the solubility of Al in the β-phase is significant [33]. For this reason, the k_i parameter was significantly higher for V than it was for Al. The highest k_V determined was for the SLM-HT specimen, whilst the cast specimen had the lowest k_V.

According to data obtained from the producers regarding the chemical composition of the alloy investigated, the amount of Fe in the Ti–6Al–4V alloy was low in comparison to the concentrations of Al and V. Approximately 1 wt.% Fe was, however, detected in the β-phase of the SLM-HT, wrought and cast specimens, caused by the diffusion of Fe (a β-stabilizing element) into the β-phase during its formation.

3.2. Electrochemical properties

Electrochemical tests were conducted in order to study the effect of the microstructure on the electrochemical properties of the SLM-HT, wrought, and cast Ti6Al4V. Electrochemical tests were performed in three different environments relevant to dental applications, namely, AS, AS with added NaF (to simulate the use of dental products such as mouthwash), and AS with lactic acid (to simulate inflammatory conditions).

Table 1 – Weight percentage (%) of Al, Ti, V, and Fe, and the elemental partition parameters for the SLM-HT, wrought, and cast specimens, as determined by EDX.

	SLM-HT			wrought			cast		
	α	β	k_i	α	β	k_i	α	β	k_i
Al	6.98 ± 0.15	4.43 ± 0.34	0.63	6.94 ± 0.05	4.39 ± 0.34	0.63	6.77 ± 0.09	4.16 ± 0.61	0.61
Ti	91.02 ± 0.17	83.87 ± 1.43	—	90.33 ± 0.12	81.16 ± 0.94	—	91.08 ± 0.19	85.52 ± 1.97	—
V	1.99 ± 0.26	10.92 ± 1.60	5.48	2.65 ± 0.12	13.40 ± 1.14	5.06	2.15 ± 0.13	9.54 ± 2.32	4.44
Fe	Not detected	0.78 ± 0.18	—	Not detected	1.04 ± 0.18	—	Not detected	0.79 ± 0.27	—
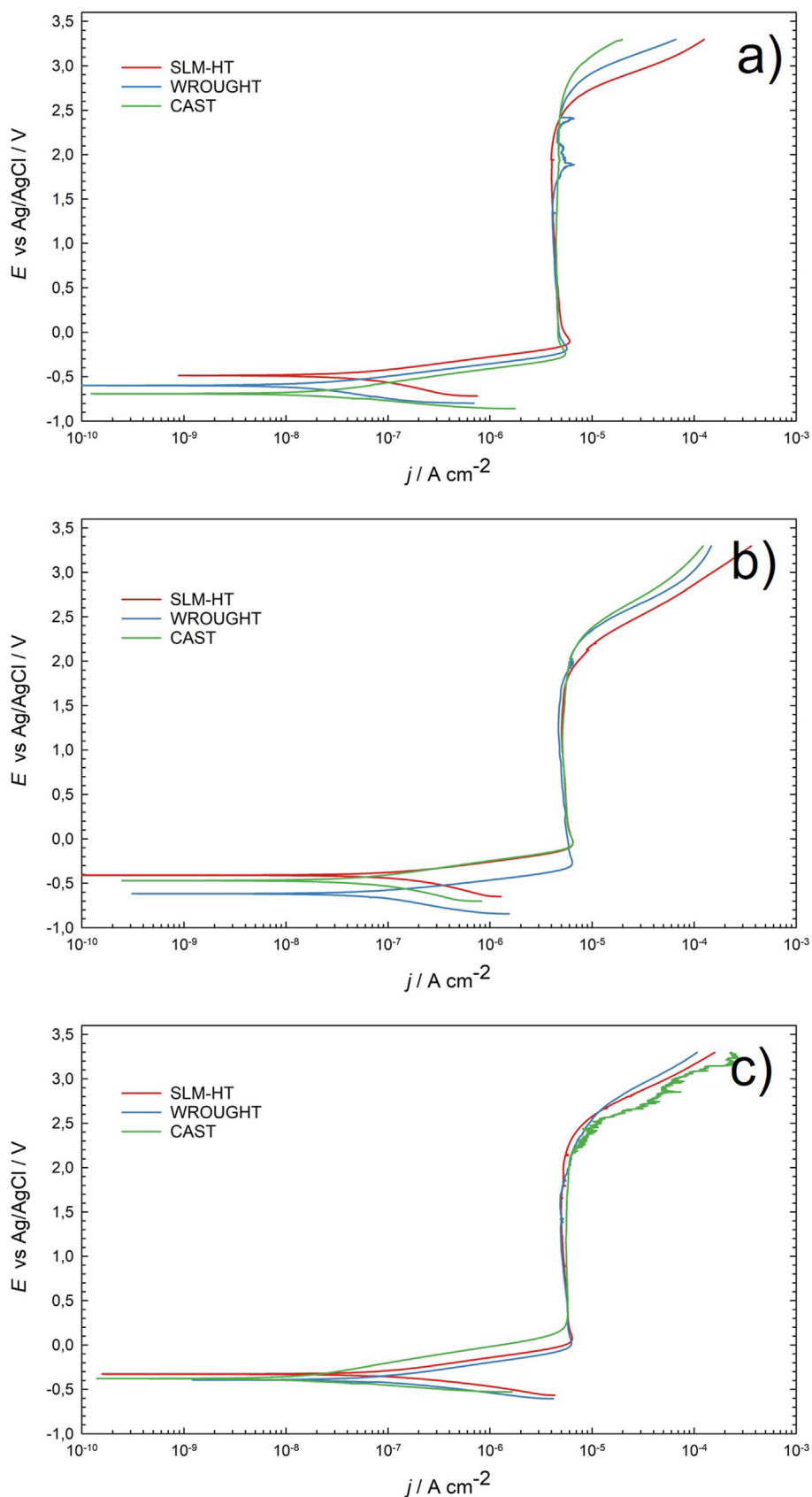
Fig. 4 − PD curves measured for the three different Ti6Al4V alloys immersed in a) AS, b) AS with 0.315 wt.% NaF or c) AS with 0.1 M lactic acid. Measurements were performed at a temperature of 37 °C and using a scan rate of 1 mV/s.

Table 2 − Electrochemical parameters deduced from E_{oc} vs time measurements, LP and PD measurements. All data are presented as the average $\pm$ standard deviation based on the measurement of three replicates.

		E_{oc} at 6800 s	LP	PD				
	Specimen	E_{oc} [mV]	R_p [M$\Omega\cdot$cm^2]	E_{corr} [mV]	j_{corr} [nA/cm^2]	E_b [V]	E_b-E_{corr} [mV]	j_{pass} [μA/cm^2]
AS	SLM-HT	-0.469 ± 0.06	0.54 ± 0.04	-0.420 ± 0.07	57.32 ± 3.29	2.54 ± 0.05	2.956 ± 0.105	4.85 ± 0.08
	wrought	-0.533 ± 0.07	0.69 ± 0.09	-0.525 ± 0.08	39.12 ± 20.70	2.73 ± 0.07	3.255 ± 0.01	4.64 ± 0.06
	cast	-0.453 ± 0.01	0.72 ± 0.12	-0.506 ± 0.04	21.85 ± 11.51	2.61 ± 0.05	3.115 ± 0.05	4.85 ± 0.01
AS with NaF	SLM-HT	-0.405 ± 0.05	0.26 ± 0.01	-0.361 ± 0.05	126.15 ± 12.00	2.04 ± 0.07	2.401 ± 0.00	5.46 ± 0.32
	wrought	-0.610 ± 0.04	0.33 ± 0.03	-0.578 ± 0.04	88.83 ± 14.05	2.23 ± 0.02	2.812 ± 0.06	5.77 ± 0.02
	cast	-0.508 ± 0.01	0.28 ± 0.03	-0.492 ± 0.01	96.12 ± 18.02	2.13 ± 0.00	2.625 ± 0.02	5.78 ± 0.01
AS with lactic acid	SLM-HT	-0.359 ± 0.01	0.27 ± 0.14	-0.330 ± 0.00	195.11 ± 99.01	2.31 ± 0.12	2.636 ± 0.10	6.38 ± 0.57
	wrought	-0.371 ± 0.02	0.34 ± 0.11	-0.363 ± 0.03	81.60 ± 7.10	2.44 ± 0.00	2.800 ± 0.15	5.90 ± 0.12
	cast	-0.335 ± 0.05	0.30 ± 0.01	-0.336 ± 0.02	133.03 ± 12.05	2.47 ± 0.08	2.839 ± 0.10	6.08 ± 0.19

Firstly, E_{oc} vs. time was measured, followed by LP and PD measurements.

PD measurements were performed on the SLM-HT, wrought, and cast Ti6Al4V specimens after 6800 s of immersion in AS, AS with NaF, and AS with lactic acid at 37 °C. The results are presented in Fig. 4. The electrochemical parameters deduced from the curves (corrosion current density, j_{corr}, passive current density, j_{pass}, passivation potential, E_{pass} and breakdown potential (E_b) are presented in Table 2. E_{oc} read at 6800 s and polarization resistance values (R_p) are also presented in Table 2.

The Ti6Al4V alloys, whether SLM-HT, wrought or cast, exhibited typical passive behaviour. For all three specimens, the low j_{corr} were determined. Moreover, low j_{pass} were also determined in the wide passive region. The E_b was estimated as the potential at which the transpassive region commenced, where a steep increase in current density can be observed (Fig. 4).

In AS, the highest j_{corr} (57.32 nA/cm^2) was measured for the SLM-HT sample, while the E_b of 2.54 V was lower than that of the wrought and cast samples (Fig. 4a). Additionally, since E_b was lowest, the width of the passive region ΔE (E_b−E_{pass}, Table 1) is subsequently narrower for the SLM-HT sample compared to the wrought and cast sample. Furthermore, the lowest R_p (0.54 MΩ cm^2) was determined for the SLM-HT sample, compared to higher values of 0.69 MΩ cm^2 and 0.72 MΩ cm^2 for the wrought and cast samples, respectively (Table 2). Very similar j_{pass} were observed for all three samples in the AS (Fig. 4a, Table 2).

In AS with 0.315 wt.% NaF (Fig. 4b), which presents a more aggressive environment compared with AS, higher j_{corr} values were determined compared with the measurements in AS, i.e. 126.15 nA/cm^2 for SLM-HT, versus lower values of 88.83 nA/cm^2 and 96.12 nA/cm^2 for the wrought and cast Ti6Al4V samples, respectively. Furthermore, the E_b values for all three specimens are approx. 500 mV at more negative potentials when compared to measurements in AS, meaning the width of the passive region is also narrower (Table 2). Conversely, the j_{pass} for all specimens are higher than the values measured in AS, since the environment of AS with flouride ions is more aggressive. Finally, for all the samples measured (SLM-HT, wrought, and cast Ti6Al4V), the R_p values are significantly lower in the AS with added NaF compared to AS (Table 2).

In the AS with added lactic acid, i.e. an acidic environment, the effect of the environment is reflected by higher j_{corr} and j_{pass} values compared to AS (Fig. 4c, Table 2). For the SLM-HT sample, the j_{corr} value was the highest amongst all of the environments tested (195.11 nA/cm^2). The width of the passive region was higher than in the AS with added NaF, meaning that this alloy mitigates localized corrosion in an AS with lactic acid better. The R_p values (Table 2) measured in AS with lactic acid are similar to those measured in the AS with added NaF. Moreover the R_p value was the lowest for the SLM-HT, compared to wrought and cast samples.

For all three types of alloy, the highest corrosion resistance, as indicated by the highest R_p value, lowest j_{pass}, and E_b at the most positive potential, was observed when the specimens were immersed to AS. The AS with added NaF represents more aggressive environment as observed from electrochemical properties. Namely, it was found previously [34] that F$^-$ from NaF have a detrimental effect on oxide film resistance to corrosion. According to the Pourbaix diagram for Ti at 37 °C, AS with lactic acid, with a pH of 2.3, causes the dissolution of Ti oxides and release of Ti-ions [35,36]. In an acidic solution with a pH of around 2.3, Al_2O_3 and V_2O_5 oxides are also unstable [35]. In all three types of alloy (SLM-HT, wrought and cast specimens − respectively), the lowest j_{pass} was measured in the AS, and the highest in the AS with lactic acid.

3.3. Surface examination following PD measurements

Surface examination of all the Ti6Al4V samples was performed by SEM following polarization in the anodic region up to 3.3 V during PD. For all the samples (cast, wrought and SLM-HT), SEM examination clearly showed a preferential attack on the β-phase (Fig. 5). This was further confirmed by post-examination performed by a confocal microscope (Fig. 6). Through this method, it was proven that the β-phase present on the surfaces of the SLM-HT, wrought and cast specimens dissolved following the PD test in the AS with lactic acid. Figs. 5 and 6 show that all β-lamellas in the SLM-HT and cast specimens were attacked. In the case of the wrought specimens, not all the intergranular β-grains deteriorated, but rather, two types of behaviour were observed; the darkest grains shown in the SEM image are those that were attacked by corrosion (as denoted by arrows, alongside the text "corroded β-phase"), whilst the unattacked β-grains are those
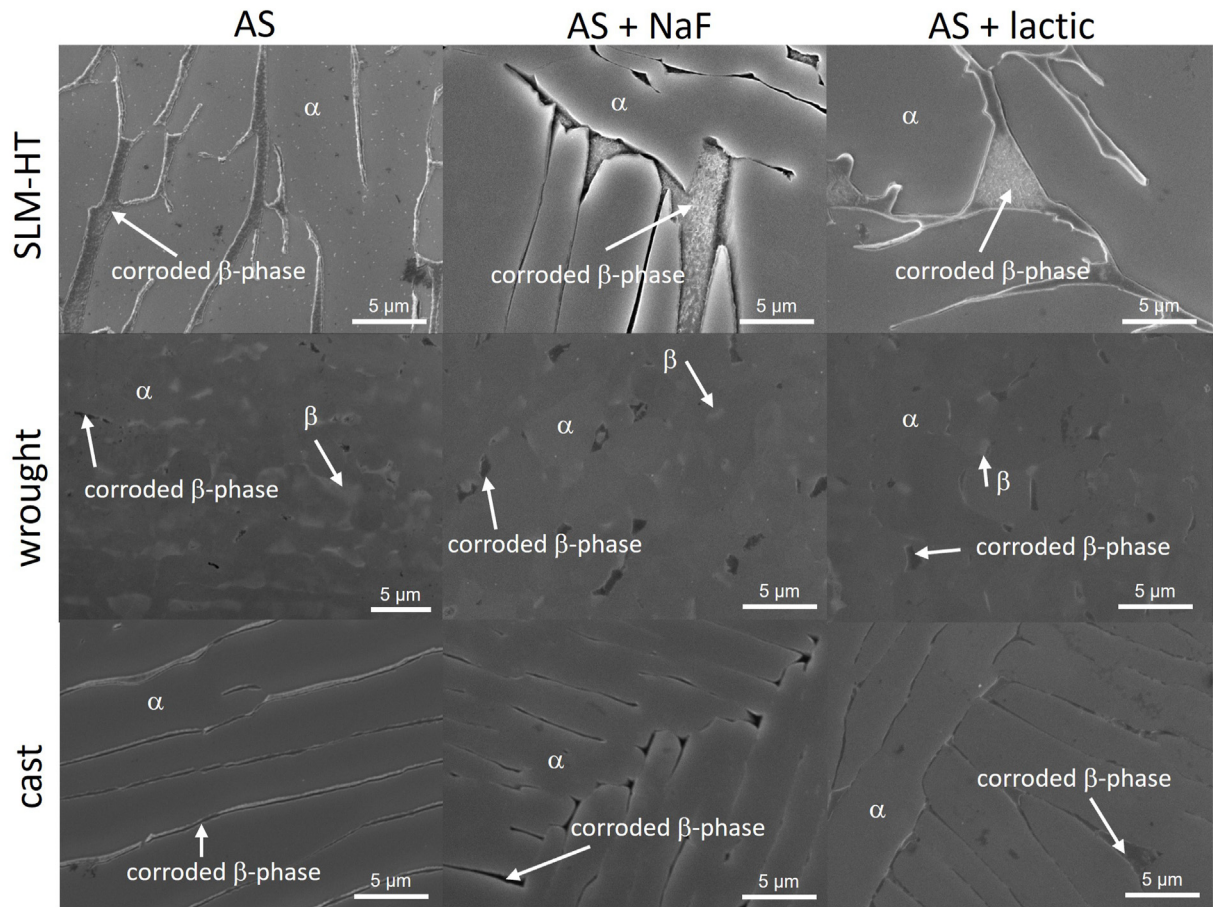
Fig. 5 — SEM images (backscattered observation) of the SLM-HT, wrought and cast samples in three different AS environments following PD polarization.

lightest in colour (as also denoted by arrows in Fig. 5, without any accompanying text). Confocal microscopy measurements reveal that, in all types of environment (AS, both with and without the addition of NaF or lactic acid), the extent of the corrosion attack on the β-phase is less than 1 μm — measured as S_z, which is maximum height, defined as the sum of the largest peak height value and the largest pit depth value within examined area (Fig. 6). Average value of S_z, obtained based on three representative measurements, were 0.72, 0.59 and 0.62 μm for SLM-HT, wrought and cast specimens, respectively.

The EDS mapping in Fig. 7 shows the surfaces of the specimens surface following measurement of the PD curve in the AS with added lactic acid; results of the EDS analysis for the other two environments are presented in the Supplementary Material Figs. S1 and S2. On the SLM-HT and cast specimens, which have a characteristic lamellar α-β microstructure, the enrichment of the β-phase with V and the impoverishment of Al can be seen. Additionally, the β-phase shows a higher concentration of oxygen compared to the α-phase, probably indicating oxidative dissolution of the V-rich β-phase [5]. Oxidation of the β-phase is uniform on the SLM-
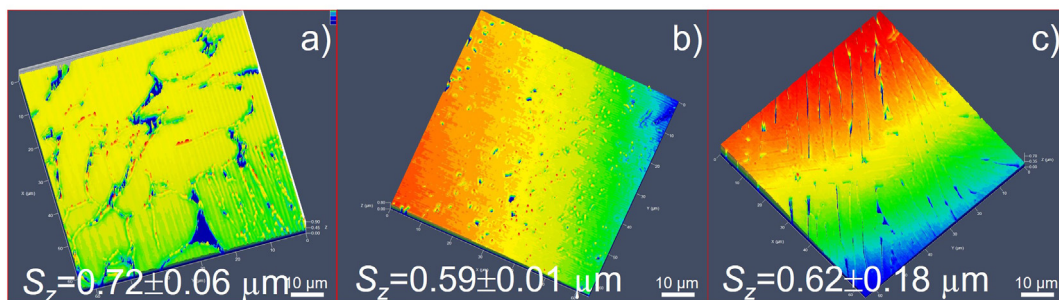
Fig. 6 — Surfaces of the a) SLM-HT, b) wrought and c) cast specimens in AS with lactic acid (pH = 2.3) following PD polarization with average value from three measurements with standard deviation.
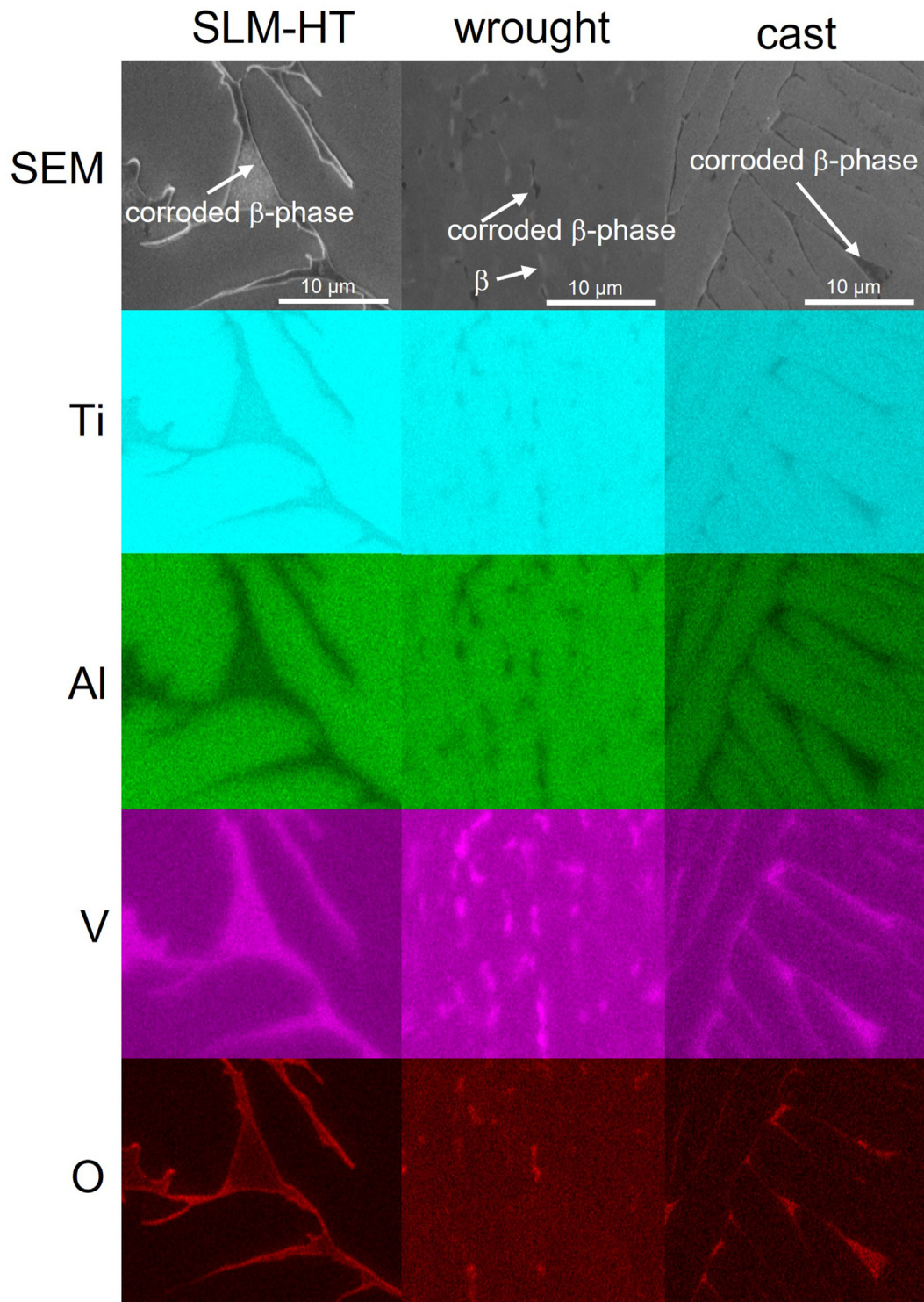
Fig. 7 − Backscattered SEM images and EDS mapping of the specimens' surfaces in AS with lactic acid following PD polarization up to 3.3 V.

HT and cast specimens, while in the case of the wrought specimen only a few of the β-grains are oxidized (see Fig. 5; oxidized β-grains are the darkest, non-oxidized grains the lightest). Similar findings were also observed in the other two types of AS (shown in Figs. S1 and S2).

3.4. ToF-SIMS analysis of oxide film formed spontaneously on $\alpha+\beta$ Ti6Al4V microstructure

ToF-SIMS images, measured in both positive and negative polarity, are shown in Figs. 8−10 for the SLM-HT, wrought and
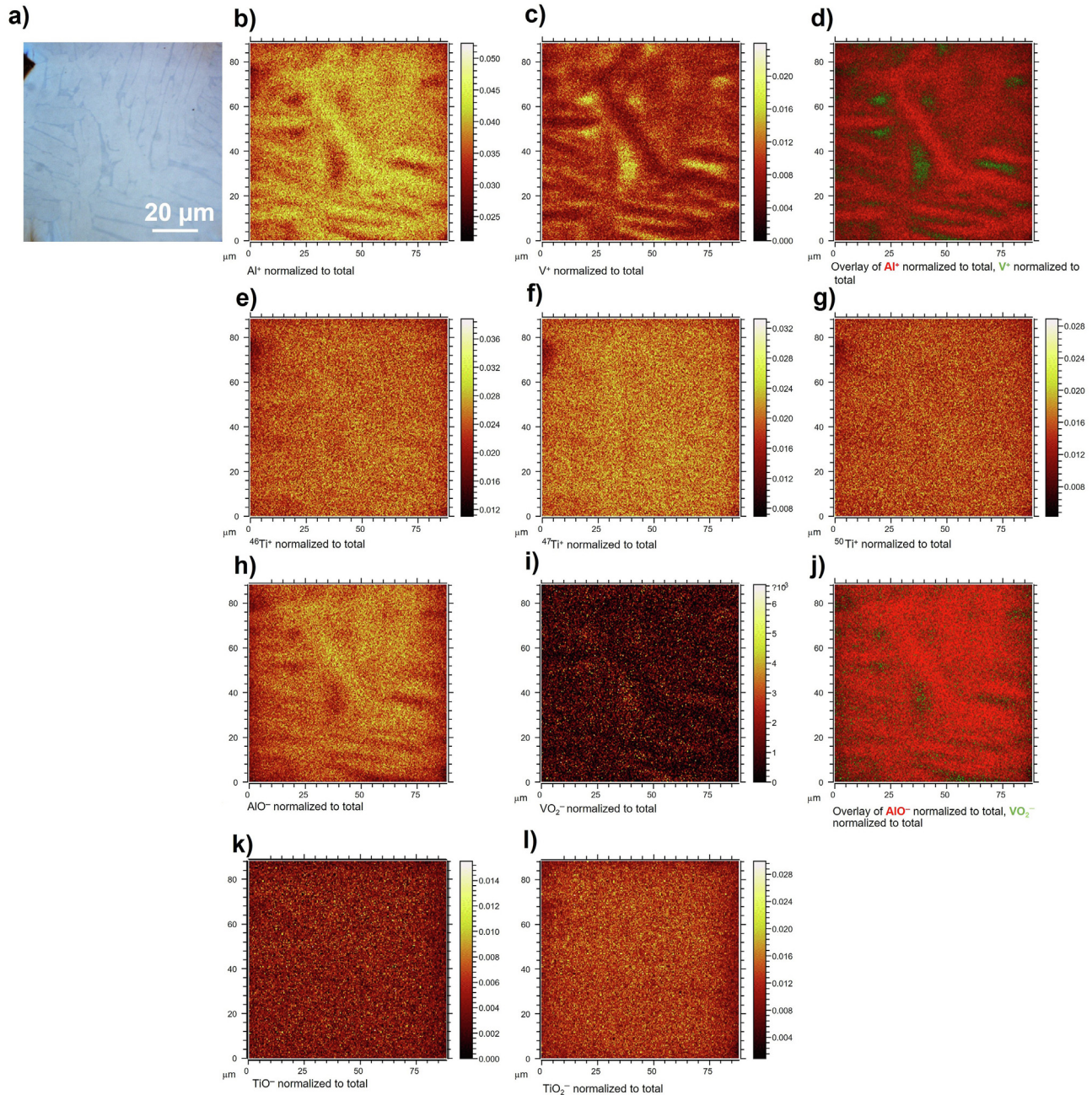
Fig. 8 − a) A metallographic optical micrograph of the analysed spot b−l) ToF-SIMS imaging of the SLM-HT specimen; b-g) ToF-SIMS imaging in positive polarity b) for Al^+, c) for V^+, d) an overlay of Al^+ (red) and V^+ (green), e) for $^{46}Ti^+$, f) for $^{47}Ti^+$ and g) for $^{50}Ti^+$; h−l) ToF-SIMS imaging in negative polarity h) for AlO^-, i) for VO_2^-, j) an overlay of AlO^- (red) and VO_2^- (green), k) for TiO^-, and l) for TiO_2^-.

cast specimens, respectively. Signals for $^{46}Ti^+$, $^{47}Ti^+$, $^{50}Ti^+$ (representing the species containing Ti) in the SLM-HT specimen are distributed homogeneously (Fig. 8e−g). Conversely, the intensity of the Al^+ signal (representing Al-containing species) is higher at the position corresponding to the α-phase (Fig. 8b), while the intensity for the V^+ signal (representing species containing V) is higher at the position of the β-phase (Fig. 8c). Moreover, in the SLM-HT specimen, the distribution of Ti oxides (represented by TiO^- and TiO_2^-, Fig. 8k,l) is homogeneous on the surface and does not depend on the

distribution/position of the microstructural phases (Fig. 8a). On the other hand, the spatial distributions of Al_2O_3 (represented by the AlO^- signal) and VO_2 (represented by the VO_2^- signal) are dependent on the underlying microstructure. Namely, the surface concentration of Al_2O_3 is higher in the α-phase (Fig. 8h), while the surface concentration of VO_2 (Fig. 8i) is higher in the β-phase. An overlay of Al_2O_3 and VO_2 is presented in Fig. 8j.

ToF-SIMS analysis for the wrought specimen is shown in Fig. 9a, which consists of homogeneous and fine equiaxed α-
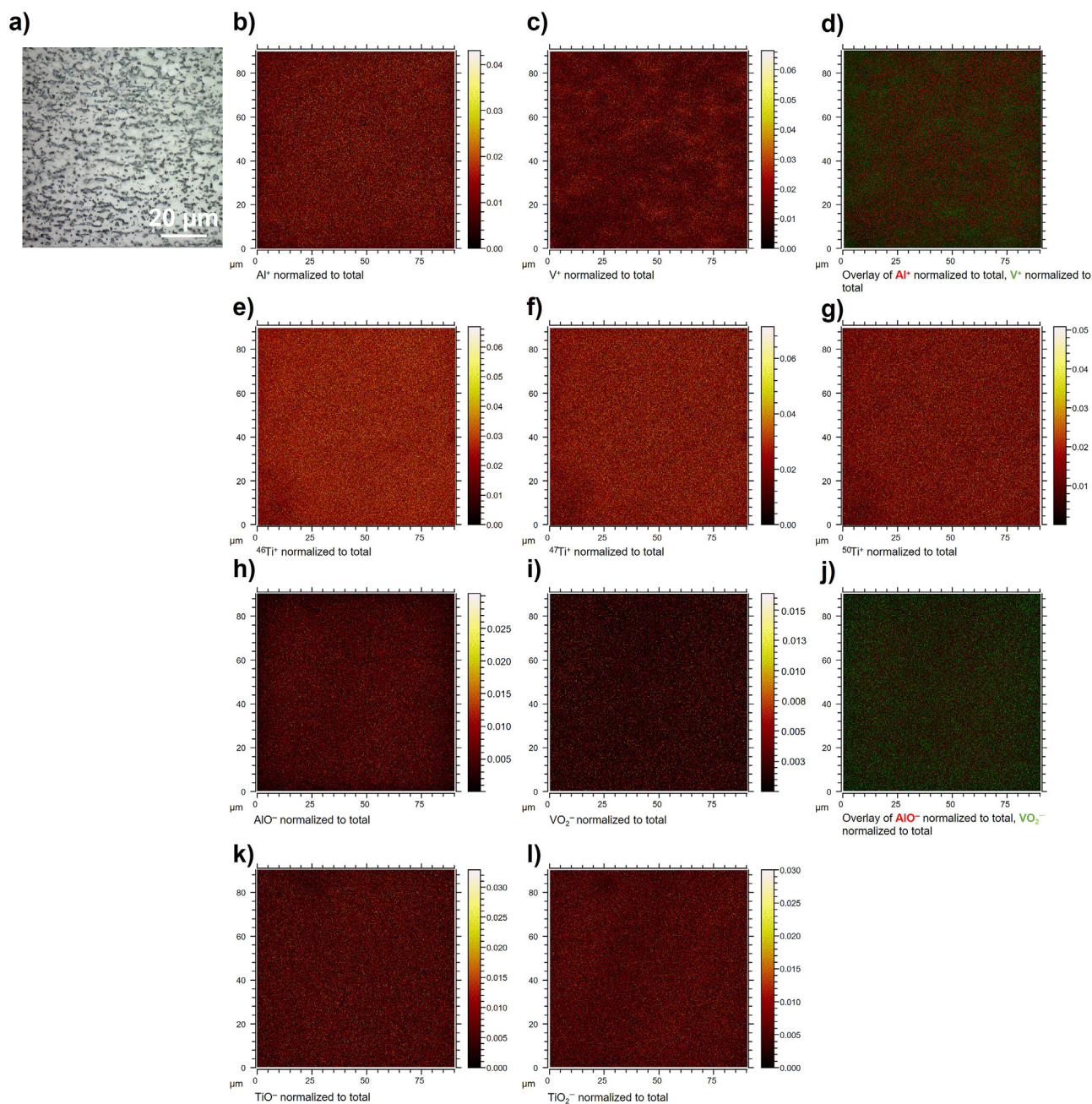
Fig. 9 – a) A metallographic optical micrograph of the analysed spot, b–l) ToF-SIMS imaging of the wrought specimen; b-g) ToF-SIMS imaging in positive polarity b) for Al^+, c) for V^+, d) an overlay of Al^+ (red) and V^+ (green), e) for $^{46}Ti^+$, f) for $^{47}Ti^+$ and g) for $^{50}Ti^+$; h–l) ToF-SIMS imaging in negative polarity h) for AlO^-, i) for VO_2^-, j) an overlay of AlO^- (red) and VO_2^- (green), k) for TiO^-, and l) for TiO_2^-.

phase with β-phase on grain boundaries. Fig. 9b,e,f,g show a homogeneous distribution of Al- and Ti-containing species. No spatial clustering of these species was present. ToF-SIMS imaging in positive polarity show that the V-species have slightly less homogeneous distribution (Fig. 9c). The latter is not connected with the microstructure distribution. On the other hand, clustering of Al_2O_3 and VO_2 oxide (represented by the corresponding signals in Fig. 9h and I) on α- or β-phase was not present.

ToF-SIMS analysis for the cast specimen is shown in Fig. 10b–m. The sample consists of alternate thin α-phase

lamellas (around 1 μm thick) and β-phase (significantly thinner than the α-phase) (Fig. 10a), with the metals and their oxides investigated being distributed homogenously. No spatial clustering of the Al-containing and V-containing species, Al_2O_3, and VO_2 occurred (Fig. 10b,c,h,i). The lower intensity for in the bottom half of the area when analysed in negative polarity is most likely due to the presence of carbonaceous contamination on the topmost position of the alloy's surface (represented by the C^- signal in Fig. 10m). The homogeneous distribution of the α- and β-phases in cast specimen most likely suppresses any clustering of the Al_2O_3 and
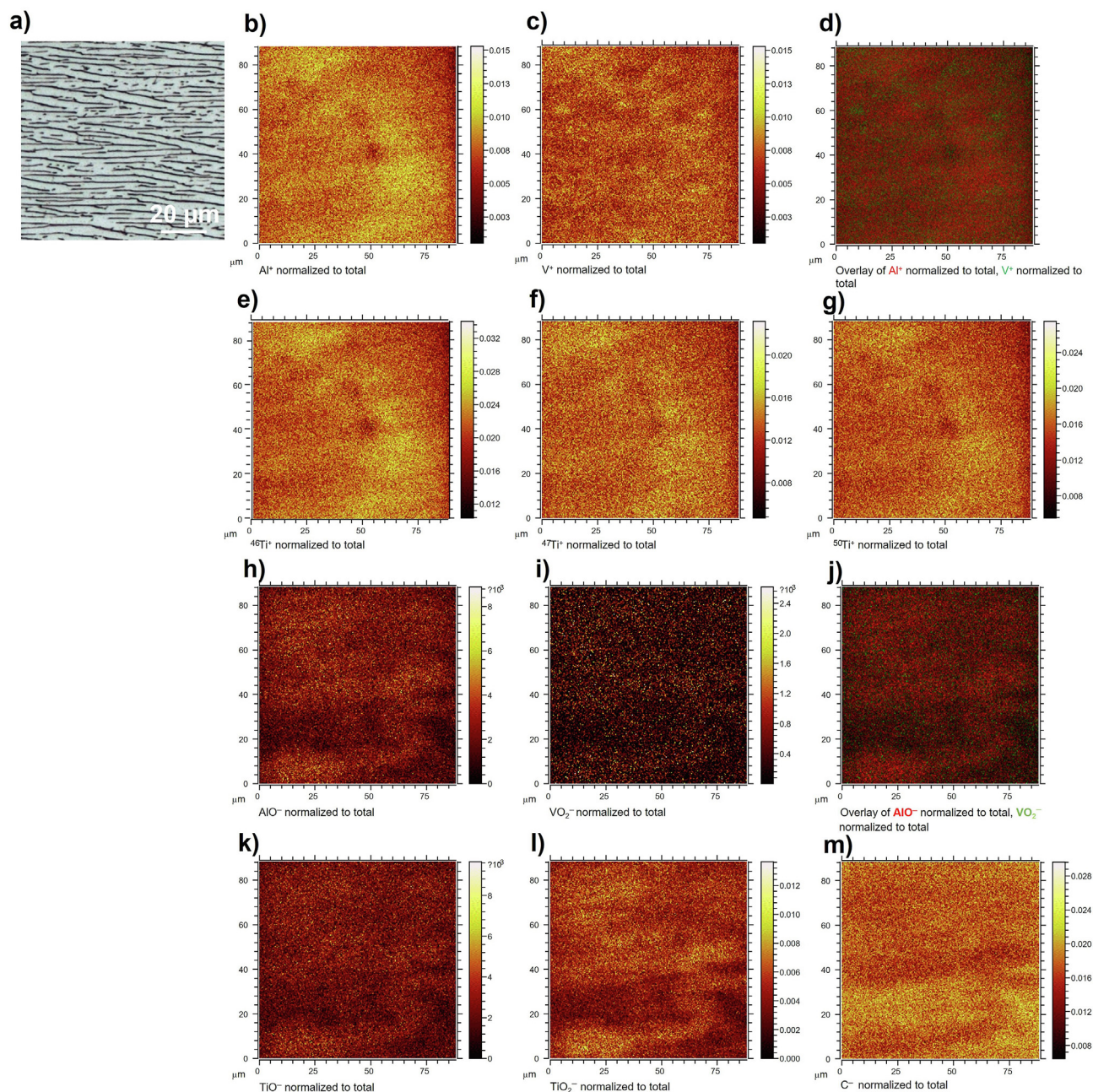
Fig. 10 — a) A metallographic optical micrograph of the analysed spot and **b—m)** ToF-SIMS imaging of the cast Specimen; **b—g)** ToF-SIMS imaging in positive polarity (b) for Al^+, c) for V^+, d) an overlay of Al^+ (red) and V^+ (green), e) for $^{46}Ti^+$, f) for $^{47}Ti^+$ and g) for $^{50}Ti^+$); **h-m)** ToF-SIMS imaging in negative polarity (h for AlO^-, i) for VO_2^-, j) an overlay of AlO^- (red) and VO_2^- (green), k) for TiO^-, l) for TiO_2^-, and m) for the C^- signal). All signals were normalized to the total ion image.

VO_2 oxide on the α- or β-phase, respectively. Of the alloys containing α+β phases, the β-phase content is highest in the SLM-HT specimen but, its distribution is also the most heterogeneous and the partitioning coefficient, k_V, the highest in this alloy.

4. Discussion

It can be concluded from the electrochemical measurements that the SLM-HT Ti6Al4V alloy exhibited worse corrosion properties than the wrought and cast Ti6Al4V samples, as observed from the j_{corr} and R_p values as well as the potential width of the passive region. In a more aggressive environment, i.e in AS with added NaF or with added lactic acid, the corrosion properties (j_{corr}, j_{pass}, and R_p) worsened for all samples, while the SLM-HT sample had still lower corrosion resistance compared with cast and wrought Ti6Al4V.

Microscopic analysis carried out after the anodic polarization up to 3.3 V confirmed that the V-rich β-phase was more susceptible to corrosion. Based on these observations, it can be deduced that V oxide formed on the β-phase, but no

corrosion damage was observed on any other surface. Many reports can be found in the literature explaining why this alloy displays such corrosion behavior. According to Metikoš-Huković et al. [27], V added to Ti-alloy, in physiological Hank's solution forms discrete clusters of V oxide embedded in the oxide film of Ti6Al4V alloy, which decreases its corrosion resistance and makes it less corrosion resistant than pure Ti or Ti alloyed with Nb. Another study [37], however, claims the opposite - that an increase in the β-phase content will increase the corrosion resistance of Ti−6Al−4V alloy in oral saliva. In our study, the highest amount of β-phase was found in the SLM-HT specimen, and the lowest in the wrought specimen.

Research by Atapour et al. [33,38] emphasized the elements' partitioning between α- and β-phases as a key parameter in determining the corrosion resistance of Ti alloys in a deaerated 5 M HCl. Neto et al. [39] claimed that the elemental partitioning - namely, a large difference in V concentration between the α- and β-grains - is the main reason for galvanic corrosion. Chen et al. [5] reported preferential dissolution of the α-phase at the E_{OC} condition in phosphate-buffered AS with the addition of NaF, and oxidative dissolution of the β-phase and the promotion of V release under the condition of applied potential.

The partitioning parameter, k_i, calculated for Al was almost identical in all the alloys investigated in our study (Table 1). Differences occur in the partitioning parameter of V (k_V), whereby the β-phase contains 5.5 times more V than the α-phase in the SLM-HT specimen, 5 times more in the wrought sample and 4.5 times more in the cast specimen (Table 1). This result confirms previous findings [33] suggesting that, in Ti6Al4V alloys containing α+β, a microstructure with a higher k_V is less resistant to corrosion.

It is assumed that the synergy between the content and aspect ratio of the β-phase, the partitioning coefficient, k_V, (presented together with electrochemical parameters in the Table) determines the difference in the corrosion resistance of the various Ti6Al4V alloys tested. SEM observation following the PD tests (see Fig. 5) revealed interesting behaviour in the wrought specimen, in which not all the β-phase grains were corroded at the end of the PD test at 3.3 V. It is most likely that the distribution of this phase in the microstructure, and its aspect ratio (the β-phase is almost equiaxed), plays an important role in the corrosion resistance. In addition, the wrought specimen exhibited an extremely fine microstructure with a very low grain size. It was reported previously [40] that in passive materials, where the passive current density does not exceed 10 μA cm^{-2}, the corrosion rate decreases as the density of the grain boundaries increases. In addition, it is assumed that a higher grain boundary density leads to a denser passive film, with fewer defects [25].

According to the study by Zhou et al. [37], the passive film of a wrought Ti6Al4V alloy is denser and thinner than the same alloy manufactured by laser metal deposition, with a higher oxygen vacancy concentration and a lower vacancy diffusion coefficient, leading to better corrosion resistance overall. The researchers attributed this to the higher β-phase content. In a study by Metikoš-Huković [41], localized corrosion of a Ti6Al4V alloy correlated with the dissolution of V at the film/electrolyte interface, which was attributed to the generation of cation vacancies and their diffusion through the film. It was suggested that one of the reasons for this was the difference between the ionic and covalent radii of Ti and V, which caused an increase in the concentration of defects and a subsequent reduction in its resistance to corrosion. According to Atapour et al. [33], the difference in chemical composition between the α- and β-phases of a Ti6Al4V alloy caused potential differences between the two phases in HCl, leading to the preferential dissolution of the V-rich β-phase. Qin et al. [25], on the other hand, noted that passivation was faster in the primary α-phase of a Ti6Al4V alloy, due to its higher Al content. Since there is less Al in the β-phase, the concentration of oxygen vacancies is lower, resulting in the passive film having a slower growth rate at the surface of the β-phase. These researchers reported that the non-uniform nature of the passive film was due to inconsistent growth, which reduced the corrosion resistance of alloys with elemental partitioning in comparison to those where the alloying elements were evenly distributed, such that the effect described previously did not occur.

The passive film of a Ti-alloy is an n-type semiconductor [33,37,41], primarily consisting of TiO$_2$, with a small amount of Al$_2$O$_3$ and an even lower amount of V oxides. The preferential formation of TiO$_2$ over Al$_2$O$_3$ in a Ti6Al4V alloy can be attributed to the higher reactivity of Ti, which leads to the initial formation of TiO$_2$ as a protective layer, and the slower oxidation rate of Al, thus limiting the formation of a thicker layer of Al$_2$O$_3$. The standard Gibbs free energy for the formation of V$_2$O$_5$ at room temperature and atmospheric pressure is more positive than for Ti and Al oxides, and therefore, the formation of V oxides is less preferable [42]. The more positive Gibbs free energy for the V oxide also indicates its lower stability; its thermodynamic stability is not, however, the only reason for the destabilization of the oxide film. Additional causes could be the oxidation state of the V oxides, its crystal structure and its reactive nature.

This study shows that the Al and V oxides were unevenly distributed in the SLM-HT specimen, as shown in Fig. 8, where results of the ToF-SIMS investigation are presented. In contrast to Al, V, and their oxides, the Ti oxides were evenly distributed. A non-uniform oxide layer can significantly contribute to the preferential dissolution of V oxide in oxide film [41] and formation of mainly point defects (cation and oxygen vacancies, and interstitials) [25,43]. In our study, despite similar partitioning coefficients, an uneven distribution of oxides was not observed in the wrought and cast specimens. The findings from Atapour [33] and Qin [25], suggesting that the partitioning of alloying elements reduces resistance to corrosion in both phases of a Ti6Al4V alloy, cannot be completely confirmed by our study. It can be assumed that, in addition to the partitioning coefficient, there must be one or more additional parameter(s) that play an important role - namely the size and shape of the β-phase, and its local quantity in comparison to the neighbouring α-phase. Due to the high concentration of V in the β-phase, and above all, its size and shape with respect to the α-phase (thickness of β-lamelles locally the same as for α), the formation rate of V oxide was higher than that of Al oxide formation, which creates an uneven distribution of oxides at the surface. In the wrought and cast samples, individual areas of the β-phase are

far more isolated from one another at the micro level than in the SLM-HT sample and therefore all contributing oxides in the oxide film formed at an even rate. It can be assumed that, in the case of the wrought and cast specimens, where the β-phase was "isolated" in the microstructure, fewer defects in the film associated with V were present than in the case of the SLM-HT specimen, where, at the micro level the β-phase was present to the same degree as the α-phase.

5. Conclusions

The corrosion properties of Ti6Al4V alloys manufactured in different ways (SLM-HT, wrought, and cast) were investigated in this study, with a special focus on correlating corrosion resistance to different types of α+β microstructures. Amongst the various α+β Ti6Al4V alloys tested, corrosion resistance was higher for wrought and cast specimens compared to SLM-HT sample. The latter is attributed to the distribution of α- and β-phases in the microstructure and the amount of β-phase present.

Based on the microstructural investigation, electrochemical testing, analysis of the elemental distribution in the microstructure, and ToF-SIMS imaging, the following conclusions, that indicate the importance of microstructure design, can be made:

- The composition of the passive film is very different on different types of microstructures.
- Clustering of V oxide was observed above the wider β-phase lamellas, and clustering of Al oxide above α-phase, present in the SLM-HT specimen. This effect was not observed above the fine β-plates/thicker α-phase of the cast specimen and on the evenly-distributed fine equiaxed β-phase on grains of α-phase of the wrought alloy.
- The clustering of Al and V oxides observed in the SLM-HT specimen makes its oxide film less resistant to corrosion. As a result, this type of β-phase in an α+β Ti6Al4V alloy with V oxide clusters which in corrosive environment preferentially dissolves, is less corrosion resistant.
- Uneven distribution of Al and V oxides in α+β Ti6Al4V oxide film depends not only on the amount of β-phase, but also upon width/length ratio of β-phase (shape) and local distribution of α and β phases on the surface.

Author contribution

M. Bajt Leban: Formal Analysis, Writing (Original Draft, Review & Editing), **T. Kosec:** Formal Analysis, Writing (Original Draft, Review & Editing), Funding acquisition, **M. Finšgar:** Formal Analysis, Writing (Original Draft, Review & Editing), Funding acquisition.

Data availability

The data that support the findings of this study are available from the corresponding authors upon reasonable request.

Declaration of Competing Interest

The authors declare that they have no known competing financial interests or personal relationships that could have appeared to influence the work reported in this paper.

Acknowledgments

Appendix A. Supplementary data

Supplementary data to this article can be found online at https://doi.org/10.1016/j.jmrt.2023.10.082.

REFERENCES

[1] Leyens C, Peters M, editors. Titanium and titanium alloys: fundamentals and applications. Weinheim; Chichester: Wiley-VCH; John Wiley; 2003. distributor.

[2] Lütjering G, Williams JC. Titanium. 2nd ed. Berlin; New York: Springer; 2007.

[3] Telegdi J, Shaban A, Vastag G. Biocorrosion—steel. Encyclopedia of interfacial chemistry. Elsevier; 2018. p. 28—42. https://doi.org/10.1016/B978-0-12-409547-2.13591-7.

[4] Zhang L, Chen L. A review on biomedical titanium alloys: recent progress and prospect. Adv Eng Mater 2019;21:1801215. https://doi.org/10.1002/adem.201801215.

[5] Chen X, Shah K, Dong S, Peterson L, Callagon La Plante E, Sant G. Elucidating the corrosion-related degradation mechanisms of a Ti-6Al-4V dental implant. Dent Mater 2020;36:431—41. https://doi.org/10.1016/j.dental.2020.01.008.

[6] Joanna Locha HK. Influence of fluoride ions in artificial saliva solution to corrosion behavior of Ti-6Al-4V and Ti-10Mo-4Zr titanium alloys. J Cast Mater Eng 2018;2:5. https://doi.org/10.7494/jcme.2018.2.3.57.

[7] Souza JCM, Apaza-Bedoya K, Benfatti CAM, Silva FS, Henriques B. A comprehensive review on the corrosion pathways of titanium dental implants and their biological adverse effects. Metals 2020;10:1272. https://doi.org/10.3390/met10091272.

[8] Zhang H, Man C, Dong C, Wang L, Li W, Kong D, et al. The corrosion behavior of Ti6Al4V fabricated by selective laser melting in the artificial saliva with different fluoride concentrations and pH values. Corrosion Sci 2021;179:109097. https://doi.org/10.1016/j.corsci.2020.109097.

[9] Francis H, Froes MQ. Titanium in medical and dental applications. Elsevier; 2018. https://doi.org/10.1016/C2016-0-03591-X.

[10] van Noort R. The future of dental devices is digital. Dent Mater 2012;28:3—12. https://doi.org/10.1016/j.dental.2011.10.014.

[11] Horn TJ, Harrysson OLA. Overview of current additive manufacturing technologies and selected applications. Sci Prog 2012;95:255—82. https://doi.org/10.3184/003685012X13420984463047.

[12] Revilla-León M, Özcan M. Additive manufacturing technologies used for 3D metal printing in dentistry. Curr Oral Health Rep 2017;4:201—8. https://doi.org/10.1007/s40496-017-0152-0.

[13] Dutta B, Babu S, Jared B. Science, technology and applications of metals in additive manufacturing. Amsterdam, Netherlands; Cambridge, MA: Elsevier; 2019.

[14] Sha W, Malinov S. Titanium alloys: modelling of microstructure, properties and applications. Boca Raton, Fla.: CRC Press; 2009.

[15] Jaber H, Kónya J, Kulcsár K, Kovács T. Effects of annealing and solution treatments on the microstructure and mechanical properties of Ti6Al4V manufactured by selective laser melting. Materials 2022;15:1978. https://doi.org/10.3390/ma15051978.

[16] Motyka M. Martensite Formation and decomposition during traditional and AM processing of two-phase titanium alloys—an overview. Metals 2021;11:481. https://doi.org/10.3390/met11030481.

[17] Dehnavi V, Henderson JD, Dharmendra C, Amirkhiz BS, Shoesmith DW, Noël JJ, et al. Corrosion behaviour of electron beam melted Ti6Al4V: effects of microstructural variation. J Electrochem Soc 2020;167:131505. https://doi.org/10.1149/1945-7111/abb9d1.

[18] Nastac L, Gungor MN, Ucok I, Klug KL, Tack WT. Advances in investment casting of Ti—6Al—4V alloy: a review. Int J Cast Metals Res 2006;19:73—93. https://doi.org/10.1179/136404605225023225.

[19] Duffó GS, Castillo EQ. Development of an artificial saliva solution for studying the corrosion behavior of dental alloys. Corrosion 2004;60:594—602. https://doi.org/10.5006/1.3287764.

[20] Bocchetta P, Chen L-Y, Tardelli JDC, Reis AC dos, Almeraya-Calderón F, Leo P. Passive layers and corrosion resistance of biomedical Ti-6Al-4V and β-Ti alloys. Coatings 2021;11:487. https://doi.org/10.3390/coatings11050487.

[21] Apaza-Bedoya K, Tarce M, Benfatti CAM, Henriques B, Mathew MT, Teughels W, et al. Synergistic interactions between corrosion and wear at titanium-based dental implant connections: a scoping review. J Periodontal Res 2017;52:946—54. https://doi.org/10.1111/jre.12469.

[22] Cordeiro JM, Barão VAR. Is there scientific evidence favoring the substitution of commercially pure titanium with titanium alloys for the manufacture of dental implants? Mater Sci Eng C 2017;71:1201—15. https://doi.org/10.1016/j.msec.2016.10.025.

[23] Avelar-Batista Wilson JC, Banfield S, Housden J, Olivero C, Chapon P. On the response of Ti—6Al—4V and Ti—6Al—7Nb alloys to a Nitron-100 treatment. Surf Coating Technol 2014;260:335—46. https://doi.org/10.1016/j.surfcoat.2014.11.034.

[24] Noronha Oliveira M, Schunemann WVH, Mathew MT, Henriques B, Magini RS, Teughels W, et al. Can degradation products released from dental implants affect peri-implant tissues? J Periodontal Res 2018;53:1—11. https://doi.org/10.1111/jre.12479.

[25] Qin T, Lin X, Yu J, Wang M, Guo P, Li J, et al. Performance of different microstructure on electrochemical behaviors of laser solid formed Ti—6Al—4V alloy in NaCl solution. Corrosion Sci 2021;185:109392. https://doi.org/10.1016/j.corsci.2021.109392.

[26] Pal S, Finšgar M, Bončina T, Lojen G, Brajlih T, Drstvenšek I. Effect of surface powder particles and morphologies on corrosion of Ti-6Al-4 V fabricated with different energy densities in selective laser melting. Mater Des 2021;211:110184. https://doi.org/10.1016/j.matdes.2021.110184.

[27] Milošev I, Metikoš-Huković M, Strehblow H-H. Passive film on orthopaedic TiAlV alloy formed in physiological solution investigated by X-ray photoelectron spectroscopy. Biomaterials 2000;21:2103—13. https://doi.org/10.1016/S0142-9612(00)00145-9.

[28] Kosec T, Močnik P, Legat A. The tribocorrosion behaviour of NiTi alloy. Appl Surf Sci 2014;288:727—35. https://doi.org/10.1016/j.apsusc.2013.10.116.

[29] Vrancken B, Thijs L, Kruth J-P, Van Humbeeck J. Heat treatment of Ti6Al4V produced by selective laser melting: microstructure and mechanical properties. J Alloys Compd 2012;541:177—85. https://doi.org/10.1016/j.jallcom.2012.07.022.

[30] Shahsavari M, Imani A, Schaller RF, Asselin E. Corrosion evaluation of Ti—6Al—4V manufactured by electron beam melting in Ringer's physiological solution: an in vitro study of the passive film. J Appl Electrochem 2022;52:1003—19. https://doi.org/10.1007/s10800-022-01683-0.

[31] Hamza HM, Deen KM, Haider W. Microstructural examination and corrosion behavior of selective laser melted and conventionally manufactured Ti6Al4V for dental applications. Mater Sci Eng C 2020;113:110980. https://doi.org/10.1016/j.msec.2020.110980.

[32] Safdar A, Wei L-Y, Snis A, Lai Z. Evaluation of microstructural development in electron beam melted Ti-6Al-4V. Mater Char 2012;65:8—15. https://doi.org/10.1016/j.matchar.2011.12.008.

[33] Atapour M, Pilchak A, Frankel GS, Williams JC, Fathi MH, Shamanian M. Corrosion behavior of Ti-6Al-4V with different thermomechanical treatments and microstructures. Corrosion 2010;66. https://doi.org/10.5006/1.3452400. 065004-065004—9.

[34] Leban MB, Kosec T, Finšgar M. Corrosion characterization and ion release in SLM-manufactured and wrought Ti6Al4V alloy in an oral environment. Corrosion Sci 2022;209:110716. https://doi.org/10.1016/j.corsci.2022.110716.

[35] Pourbaix M. Atlas of electrochemical equilibria in aqueous solutions. Houston, Tex: National Assoc. of Corrosion Engineers; 1974. u.a.

[36] Bhola R, Bhola SM, Mishra B, Olson DL. Electrochemical behavior of titanium and its alloys as dental implants in normal saline. Res Lett Phys Chem 2009;2009:1—4. https://doi.org/10.1155/2009/574359.

[37] Zhou X, Xu D, Geng S, Fan Y, Yang C, Wang Q, et al. Microstructural evolution and corrosion behavior of Ti—6Al—4V alloy fabricated by laser metal deposition for dental applications. J Mater Res Technol 2021;14:1459—72. https://doi.org/10.1016/j.jmrt.2021.07.006.

[38] Atapour M, Pilchak AL, Frankel GS, Williams JC. Corrosion behavior of β titanium alloys for biomedical applications. Mater Sci Eng C 2011;31:885—91. https://doi.org/10.1016/j.msec.2011.02.005.

[39] Neto M, Radice Lampe S, Hall D, Frisch N, Mathew M, Fischer A, et al. Microstructure and electrochemical behavior of contemporary Ti6Al4V implant alloys. J Bio Tribocorros 2022;8. https://doi.org/10.1007/s40735-021-00623-3.

[40] Ralston KD, Birbilis N, Davies CHJ. Revealing the relationship between grain size and corrosion rate of metals. Scripta Mater 2010;63:1201—4. https://doi.org/10.1016/j.scriptamat.2010.08.035.

[41] Metikoš-Huković M, Kwokal A, Piljac J. The influence of niobium and vanadium on passivity of titanium-based implants in physiological solution. Biomaterials 2003;24:3765—75. https://doi.org/10.1016/S0142-9612(03)00252-7.

[42] The Ellingham diagram n.d. https://www.doitpoms.ac.uk/tlplib/ellingham_diagrams/ellingham.php (accessed June 1, 2023).

[43] Macdonald D. The history of the Point Defect Model for the passive state: a brief review of film growth aspects. Electrochimica Acta 2011;56:1761—72. https://doi.org/10.1016/j.electacta.2010.11.005.